catalysts

MDPI

*Article*

# Changes in $CO_2$ Adsorption Affinity Related to Ni Doping in FeS Surfaces: A DFT-D3 Study

**Aleksandar Živković [1,*], Michiel Somers [1], Eloi Camprubi [1], Helen E. King [1], Mariette Wolthers [1,*] and Nora H. de Leeuw [1,2,3,*]**

[1] Department of Earth Sciences, Utrecht University, Princetonlaan 8a, 3584CB Utrecht, The Netherlands; michiel.somers93@gmail.com (M.S.); e.camprubicasas@uu.nl (E.C.); H.E.King@uu.nl (H.E.K.)
[2] School of Chemistry, University of Leeds, Leeds LS2 9JT, UK
[3] School of Chemistry, Cardiff University, Park Place, Cardiff CF10 3AT, UK
* Correspondence: a.zivkovic@uu.nl (A.Ž.); m.wolthers@uu.nl (M.W.); N.H.Deleeuw@uu.nl (N.H.d.L.)

**Abstract:** Metal sulphides constitute cheap, naturally abundant, and environmentally friendly materials for energy storage applications and chemistry. In particular, iron (II) monosulphide (FeS, mackinawite) is a material of relevance in theories of the origin of life and for heterogenous catalytic applications in the conversion of carbon dioxide ($CO_2$) towards small organic molecules. In natural mackinawite, Fe is often substituted by other metals, however, little is known about how such substitutions alter the chemical activity of the material. Herein, the effect of Ni doping on the structural, electronic, and catalytic properties of FeS surfaces is explored via dispersion-corrected density functional theory simulations. Substitutional Ni dopants, introduced on the Fe site, are readily incorporated into the pristine matrix of FeS, in good agreement with experimental measurements. The $CO_2$ molecule was found to undergo deactivation and partial desorption from the doped surfaces, mainly at the Ni site when compared to undoped FeS surfaces. This behaviour is attributed to the energetically lowered *d*-band centre position of the doped surface, as a consequence of the increased number of paired electrons originating from the Ni dopant. The reaction and activation energies of $CO_2$ dissociation atop the doped surfaces were found to be increased when compared to pristine surfaces, thus helping to further elucidate the role Ni could have played in the reactivity of FeS. It is expected that Ni doping in other Fe-sulphides may have a similar effect, limiting the catalytic activity of these phases when this dopant is present at their surfaces.

**Keywords:** iron sulphides; mackinawite; density functional theory; carbon dioxide ($CO_2$) adsorption; nickel doping



**Citation:** Živković, A.; Somers, M.; Camprubi, E.; King, H.E.; Wolthers, M.; de Leeuw, N.H. Changes in $CO_2$ Adsorption Affinity Related to Ni Doping in FeS Surfaces: A DFT-D3 Study. *Catalysts* **2021**, *11*, 486. https://doi.org/10.3390/catal11040486

Academic Editor: Francis Verpoort

Received: 19 March 2021
Accepted: 8 April 2021
Published: 10 April 2021



## 1. Introduction

The production of fuels and organic molecule feedstock from captured $CO_2$ and a hydrogen source, e.g., water, using renewable energy sources is considered a promising route towards achieving a sustainable and green future [1]. For example, renewable sources often generate electrical energy that exceeds demand. This excess energy could be used to transform captured $CO_2$ to chemicals and fuels, converting this electrical energy to a store of chemical energy for future use [2–4]. In addition, the electrocatalytic reduction of $CO_2$ represents a clean and efficient way to produce valuable fuels (such as alcohols or hydrocarbons) or fuel precursors through $CO_2$ recycling [5,6]. A key requirement for an effective conversion of $CO_2$ is the development of efficient and inexpensive catalysts, which at the same time demonstrate sufficient durability, activity, and selectivity towards valuable products [7].

Transition metal sulphides constitute a group of naturally generated materials with arguably the most diverse electrical and magnetic properties available. They include materials with a variety of properties, including diamagnetic insulators (ZnS), diamagnetic semiconductors (PbS), antiferromagnetic semiconductors ($CuFeS_2$), ferrimagnetic

($Fe_7S_8$) and antiferromagnetic metallic conductors ($Fe_9S_{10}$), or Pauli paramagnetic metals ($(Ni,Fe)_9S_8$), just to name a few [8–10]. Amongst those, iron sulphides constitute a distinct group of solids and complexes that play a key role in marine systems and global biogeochemical sulphur cycles, which are central to fundamental concepts about the evolution of the Earth surface environment [11]. More importantly, they have been associated as catalysts in a number of key biochemical reactions related to Origin of Life theories [11–17], and more recently, as a potential electron source for autotrophic denitrification [18], as well as chromium [19] and vanadium removal [20]. Due to the variety in composition and structure of iron sulphides, a broad range of oxidation states is possible for both the iron and sulphur, which consequently makes these minerals remarkably reactive [8,21].

In this work, the effect of nickel substitution for iron on the catalytic properties of mackinawite (tetragonal FeS) towards $CO_2$ adsorption, activation, and reduction is assessed using calculations based on the density functional theory (DFT). Earlier studies have elucidated the interaction of mackinawite surfaces with $NO_X$ gases [22], methylamine [23], carbon dioxide [24], arsenous acid [25], cysteine [26], water [27,28], trichloroethylene [29], uranium [30], and mercury [31], amongst various other adsorbates. However, considerably less information is available in the literature on the adsorption properties of doped mackinawite. According to early studies conducted by Morse et al. [32], there is evidence that naturally formed FeS can accommodate significant concentrations of metals other than Fe, e.g., Cu, Co, and Ni. Cody et al. [16] noted that natural metal sulphides are rarely compositionally pure, rather extensive cationic substitutions are often encountered. Even a minor amount of substitution, e.g., $Ni^{2+}$ for $Fe^{2+}$ in FeS or $Mn^{2+}$ for $Zn^{2+}$ in ZnS, was postulated to induce significant changes in catalytic properties, yet the effect has not been studied in detail [21]. Kwon et al. [33] have employed DFT calculations to examine the structural effects of both substitutional and intercalated transition metals (namely Co, Ni, and Cu) incorporated into bulk FeS. The authors found that metal incorporation into mackinawite most likely occurs via substitution, which was further inferred to influence phase transformation pathways of mackinawite.

Wilkin et al. [34] examined the uptake of Ni by synthetic FeS mackinawite. Rapid and efficient Ni uptake was observed for FeS, consistent with previous studies of Hg, Pb, and Cd incorporation. Ikogou et al. [35] observed Ni(II) successfully substituting Fe(II) in the structure of biogenic mackinawite together with the possible influence of Ni on the stabilization and delay of the transformation of mackinawite into pyrite ($FeS_2$). A similar conclusion was reached by Swanner et al. [36], who noted a kinetic inhibition to the formation of pyrite in the presence of Co and Ni.

Despite the observations and expectations on the effects of Ni on the properties of mackinawite, there is little specific information on how dopants may alter its catalytic activity. The present study therefore aims to provide a detailed understanding of a Ni-doped FeS system and its potential application as a catalytic material for $CO_2$ adsorption. Some of the research questions of interest that this study aims to elucidate are:

(1) What is the energetic cost to form Ni defects in otherwise pristine surfaces of FeS?
(2) How does substitutionally incorporated Ni distribute itself across the surfaces of FeS?
(3) What influence does Ni exert on the adsorption of $CO_2$ onto the surfaces of FeS?

## 2. Computational Details

Spin-polarized density functional theory calculations were performed using the Vienna ab-initio simulation package (VASP) [37–39] with the projector-augmented wave (PAW) method and a plane-wave cut-off of 400 eV. For the PAW potentials, the valence electronic configurations used were $4s^1 3d^7$ for iron and $3s^2 3p^4$ for sulphur.

The general gradient approximation (GGA) for the exchange-correlation (XC) functional was employed within the Perdew-Burke-Ernzerhof (PBE) parametrisation [40]. Long-distance dispersion corrections were included using the D3 approach of Grimme et al. [41]. The conjugate gradient method was used for structural optimisations, with the total energy and force convergence criteria set to $10^{-5}$ eV and 0.01 eV/Å. The Brillouin zone was sam-

pled using 9 × 9 × 7 and 9 × 9 × 1 Γ-centred Monkhorst-Pack meshes for the bulk and surfaces of FeS, respectively [42]. The nickel-doped surfaces as well as the $CO_2$ adsorption and dissociation calculations were sampled on a 5 × 5 × 1 Γ-centred mesh of k-points.

The extent of charge distributions was studied using the Bader scheme, as implemented in the Henkelman code [43–45]. Graphical drawings were produced using VESTA [46]. The d-band centre was obtained using the VASPKIT program [47]. The transition states and activation barriers were determined with the climbing-image nudged elastic band (cNEB) method [48–50].

### 2.1. Defect Calculations

The formation energy of a neutral defect $E^f$ is defined as [51]:

$$E^f(D) = E_{tot}(D) - E_{tot}(H) - \sum_i n_i \mu_i,$$

where $E_{tot}(D)$ and $E_{tot}(H)$ are the respective total energies of the system with and without the defect, respectively. The value of $n_i$ represents the number of atoms of element $i$ that are added ($n_i > 0$) or removed ($n_i < 0$) from the supercell to form the defect, and $\mu_i$ is the chemical potential of element $i$, which can be written as $\mu_i = \mu_i^{elem} + \Delta\mu_i$, where $\mu_i^{elem}$ is the chemical potential of element $i$ in its standard phase, with reference to the total energy of the elementary phases at zero Kelvin (i.e., Fe(s) and $S_8$(g)).

The allowed values of $\Delta\mu_i$ are determined from a set of thermodynamic limits. The upper limit is defined through $\Delta\mu_i$, where element $i$ precipitates to its standard phase, which in this case reads metallic iron and molecular sulphur in the gas phase. Further, to avoid the formation of secondary solids, the chemical potentials must be bound by:

$$\Delta\mu_{Fe} + 2\Delta\mu_S \leq \Delta H_f(FeS_2),$$

$$3\Delta\mu_{Fe} + 4\Delta\mu_S \leq \Delta H_f(Fe_3S_4),$$

$$7\Delta\mu_{Fe} + 8\Delta\mu_S \leq \Delta H_f(Fe_7S_8),$$

with $\Delta H_f$ being the standard enthalpy of formation at zero Kelvin. The total energies of the phases competing with *FeS* were calculated using their respective unit cells. $FeS_2$ and $Fe_3S_4$ were modelled with a simple cubic cell, while $Fe_7S_8$ was modelled using the low-temperature ferrimagnetic monoclinic phase.

Finally, to maintain the thermodynamic equilibrium with *FeS*, the chemical potentials are additionally constrained by the condition:

$$\Delta\mu_{Fe} + \Delta\mu_S \leq \Delta H_f(FeS).$$

The outlined chemical potential analysis yields a Fe-rich/S-poor environment with $\Delta\mu_{Fe} = 0$, $\Delta\mu_S = -1.023$, and Fe-poor/S-rich environment with $\Delta\mu_{Fe} = -0.503$, $\Delta\mu_S = -0.519$.

Upon doping, the solubility of the Ni species is limited by the formation of the secondary phase, $FeNi_2S_4$ (the mineral violarite):

$$\Delta\mu_{Fe} + 2\Delta\mu_{Ni} + 4\Delta\mu_S \leq \Delta H_f(FeNi_2S_4),$$

where $\Delta\mu_{Ni}$ can be calculated to be 0.738 under Fe-rich/S-poor conditions and −0.016 under Fe-poor/S-rich conditions, with only the latter value being physically relevant.

### 2.2. Surface Calculations

The METADISE code [52] was employed to create the three dominant low Miller index surfaces of FeS, namely (001), (011), and (111). The surfaces were modelled as a slab of material with periodic boundary conditions in the plane direction and a vacuum layer in

the direction orthogonal to the surface. A vacuum region of at least 15 Å was tested to be sufficient to avoid interactions between the periodic slabs.

To characterise the surfaces, the surface energy ($\gamma$) as a measure of the thermodynamic stability has been calculated through the following formalism [53]:

$$\gamma_{unrelaxed} = \frac{E^{DFT}_{unrelaxed-slab} - n \times E^{DFT}_{bulk}}{2A_{slab}},$$

$$\gamma_{relaxed} = \frac{E^{DFT}_{relaxed-slab} - n \times E^{DFT}_{bulk}}{A_{slab}} - \gamma_{unrelaxed},$$

where $\gamma_{unrelaxed}$ and $\gamma_{relaxed}$ are the surface energies before and after relaxation, $E^{DFT}_{unrelaxed-slab}$, $E^{DFT}_{relaxed-slab}$, and $E^{DFT}_{bulk}$ are the DFT energies of the unrelaxed and relaxed slab and bulk respectively, $A_{slab}$ is the surface area, and $n$ is the ratio between the number of atoms in the slab and in the bulk.

The adsorption energy of $CO_2$ ($E_{ads}$) was calculated from the fully atomically relaxed geometries. The total energy of the slab with the adsorbate ($E_{slab+adsorbate}$), the energy of the adsorbate ($E_{adsorbate}$), and pristine slab energy ($E_{slab}$) are related via the following expression:

$$E_{ads} = E_{slab+adsorbate} - (E_{slab} + E_{adsorbate}),$$

where negative adsorption energy values indicate energetically favourable exothermic processes, while positive energies correspond to endothermic processes.

## 3. Results and Discussion

### *3.1. Bulk and Pristine FeS Surfaces*

Bulk mackinawite forms in a tetragonal crystal structure (space group *P*4/*nmm*, number 129), with the conventional cell containing two iron and two sulphur atoms (structure shown in Figure 1). The calculated lattice parameters (a = 3.581 Å and c = 5.011 Å) reproduce within a few percent the experimentally observed values [54], similar to the findings in earlier studies [24].

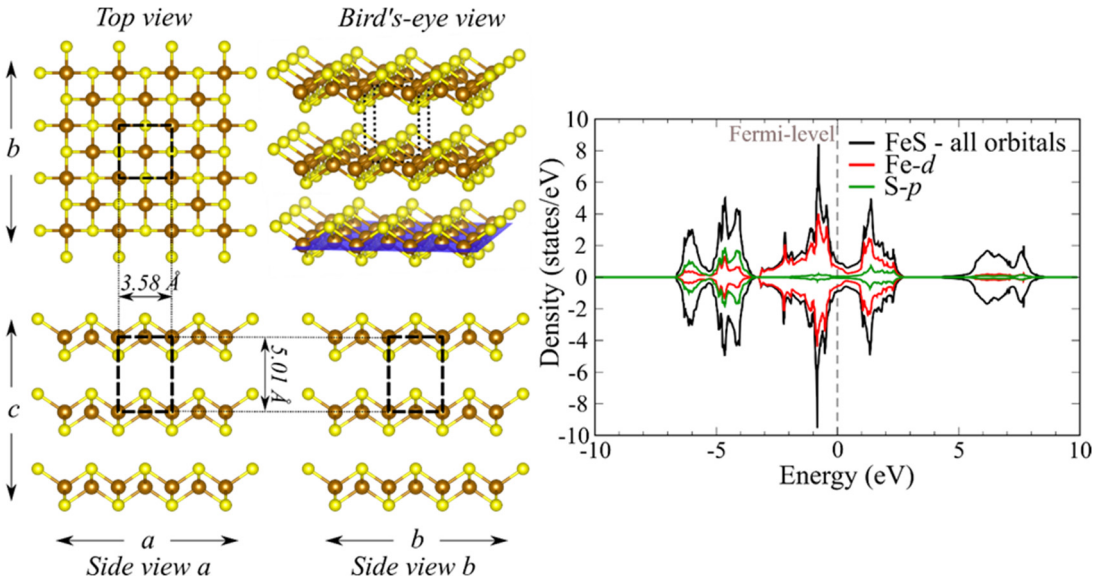


**Figure 1.** Crystal structure of bulk FeS mackinawite shown on the left. The unit cell is indicated with black striped lines, while sulphur and iron atoms are coloured yellow and brown, respectively. The total electronic densities of states, together with the orbital projected ones, are shown on the right.

The calculated relaxed surface energies of the three dominant surfaces of FeS are listed in Table 1. The obtained values match very well with the trends observed in previous

works, with the differences being attributed to the use of a disparate exchange-correlation functional and correction for long-range interactions. The (001)-S surface was found to be the dominant surface of FeS, as the creation of the surface effectively breaks only the weak Van der Waals interlayer interaction and as such does not alter the coordination number of any Fe or S atoms. This observed high stability of the (001)-S surface is also in line with earlier experimental findings [54]. Despite the high energy required to form certain surfaces (particularly the (001)-Fe termination), all surfaces were tested in subsequent defect calculations.

**Table 1.** Calculated relaxed surface energies of three low Miller index surfaces of FeS.

| Surface | Termination | Relaxed Surface Energy, $\gamma_{relaxed}$ (J/m$^2$) | Other Theoretical Works [24] |
|---|---|---|---|
| (001) | S | 0.23 | 0.19 |
| | Fe | 3.55 | N/A |
| (011) | S | 1.14 | 1.47 |
| | Fe | 1.15 | 0.95 |
| (111) | S | 1.27 | 1.51 |
| | Fe | 1.66 | 1.69 |

### *3.2. Ni-Doped FeS Surfaces*

To model FeS surfaces doped with Ni in the desired ratio of 1:5 (1 Ni atom for every 5 Fe atoms, which is accessible within the experimental regime [34,55]), 2 × 2 supercells were created from the previously relaxed systems, with several Fe atoms substituted by Ni atoms. Three possible arrangements (scenarios) were modelled: Ni atoms substituting the first layer of Fe atoms, Ni atoms replacing the second layer of Fe atoms in the slab, and Ni atoms found randomly dispersed throughout the simulation cell. A random number generator was used to obtain the dispersed distribution of Ni atoms throughout the surfaces, with the final geometries available in the Supplementary File.

The calculated formation energies of the Ni-doped FeS surface are shown in Figure 2. The first observation is that all defects have negative formation energies (with only slightly positive values in the case of the 001-S terminated surface). This indicates spontaneous substitution of Fe atoms with Ni ones, i.e., no energy investment is necessary to form the defects. This indicates that difficulties may be met in controlling the doping process when incorporating Ni into the FeS in the desired Ni:Fe ratio. Despite such seemingly unphysical results, they agree well with previous experimental studies which demonstrated a high uptake of $Ni^{2+}$ ions by mackinawite [32,34,55]. Likewise, earlier theoretical studies noted that metal substitution of Fe (by Co, Ni, and Cu) is thermodynamically more favoured over intercalation in bulk mackinawite FeS [33].

A trend amongst the (011) and (111) surfaces is noted, where the Ni dopants substituting Fe in the first layer and the ones randomly dispersed through the surface are energetically always preferred over the counterpart occurring in the first subsurface layer. Defects occupying the sub-surface layer interact strongly and induce considerable lattice relaxation in both directions along the z-axis (perpendicular to the surface), whereas defects in the first layer can more easily extend into the space above the surface. The competitive interplay between the dopants in the first layer and randomly dispersed ones explains the experimentally noted slow Ni uptake process in FeS, which indicated a combination of Ni intercalated between S-S layers and diffusion-controlled lattice penetration and structural substitution [34].

The optimised structures of the doped surfaces are shown in Figure 3. The (001)-Fe-terminated surface undergoes the most significant structural reconfiguration (in all considered scenarios) as a result of the surface accommodating the dopant atoms. The Fe and Ni atoms undergo relaxation into the surface, bridging the underlying tetrahedral sheets and forming a regular S-terminated configuration, in the case of the (001)-Fe surface doped randomly and with dopants, the second layer, which reflects the high surface energy

outlined earlier, the (001)-Fe surface requires a substantial energetic investment to form and reorganises promptly upon small perturbations. The remaining surfaces show negligible relaxation when doped with Ni, predominantly as a result of the elongated Ni-S bond lengths (compared to the initial Fe-S bonds) arising from the increased Coulomb repulsion between electrons.

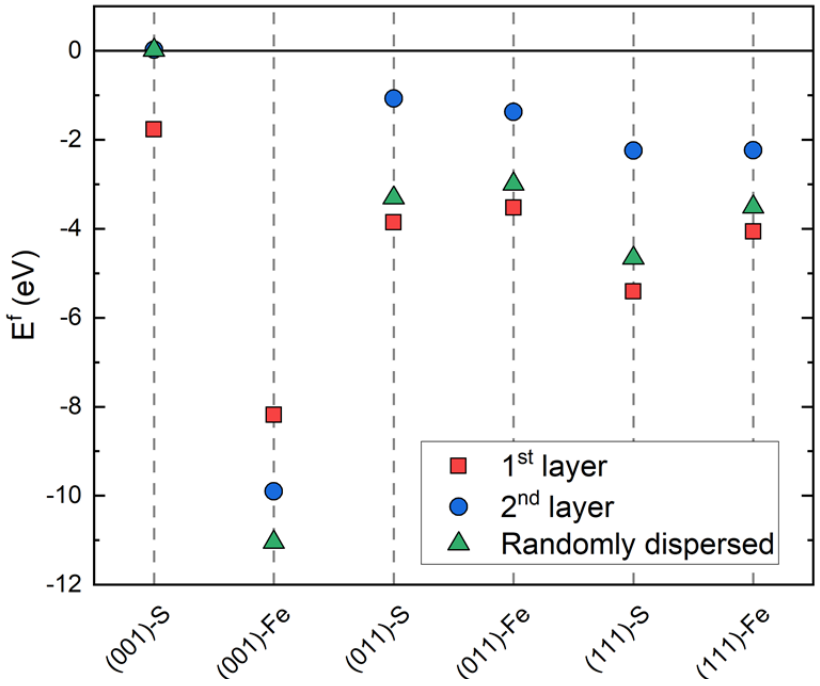


**Figure 2.** Calculated defect formation energies of selected Ni-doped FeS surfaces.

The obtained results are in good agreement and complement existing experimental findings. For example, Wilkin et al. [34] measured a slightly elongated Ni-S bond distance of (2.28 ± 0.01) Å in Ni-doped mackinawite, compared to a Fe-S distance of 2.26 Å in Ni-free mackinawite. In the same study, a coordination number of (4.04 ± 0.30) was derived for mackinawite with composition $Fe_{0.58}Ni_{0.42}S$, close to the 4-fold Fe coordination in pristine FeS. Despite these results obtained for a bulk sample of synthetic FeS and an increased Ni-content, similar behaviour of elongated Ni-S bond distances and preserved 4-fold coordination was observed for the Ni-doped surfaces of mackinawite FeS considered in this study.

### *3.3. Adsorption and Activation of $CO_2$ on Pristine vs. Ni-Doped FeS Surfaces*

The adsorption of $CO_2$ was first performed on the pristine surfaces of FeS mackinawite, to define a reference point for comparison with the Ni-doped surfaces. The single $CO_2$ molecule introduced on the (001)-S-terminated surface moved away perpendicular from the surface during the atomic relaxation and energy minimisation process, regardless of the initial placement of the molecule. The distance between the surface and the adsorbate was found to be larger than 5 Å, confirming the non-existing adsorption noted by a vanishing adsorption energy value (Table 2).

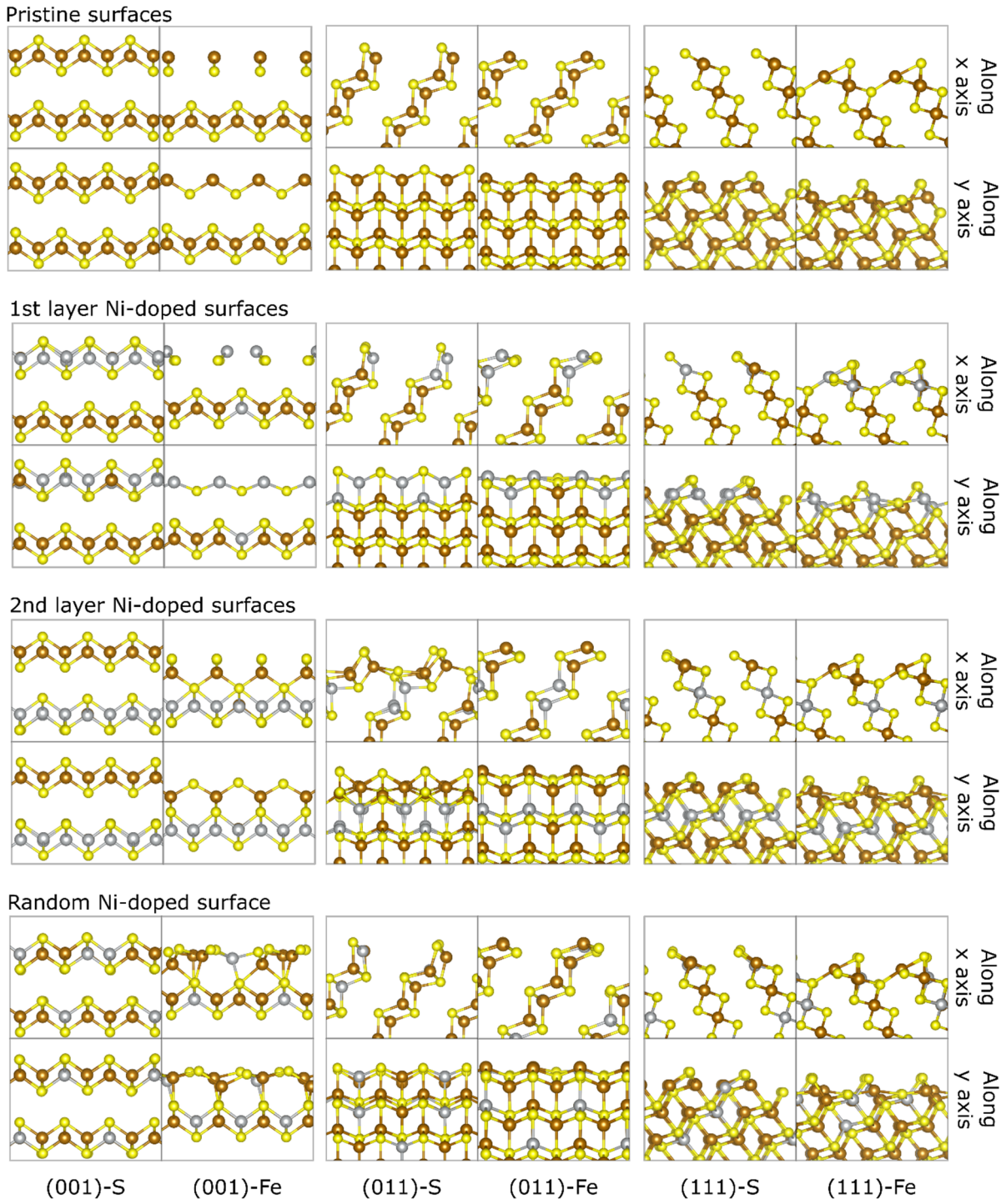


**Figure 3.** Optimised structures of the relaxed pristine as well as Ni-doped FeS surfaces of choice. Brown, yellow, and grey spheres represent iron, sulphur, and nickel atoms, respectively.

Adsorption of carbon dioxide on top of the (001)-Fe surface was tested for completeness of the results, yet no stable configuration was determined. The surface also underwent strong reorganisation, effectively turning itself into an S-terminated plane, confirming the difficulty of stabilising and achieving control over this particular surface.

In contrast to the (001) surface, $CO_2$ is found to physisorb onto the sulphur-terminated (011) and chemisorb onto the iron-terminated (011) surface of FeS mackinawite, in both cases at an exposed Fe site (Table 2). In the case of (011)-S, $CO_2$ binds solely through an O atom interacting with the exposed Fe site, leading to negligible changes in the bond

length and angles of the adsorbate. The adsorption configuration of $CO_2$ at the (011)-Fe surface matches well with the bent configuration labelled as B(III) in the work of Dzade et al. [24], where the molecule binds actively through one O and a C atom to two surface Fe atoms. The molecule also undergoes significant bending, and the O-C bond is stretched considerably, indicating possible activation (depicted in Figure 4). On the (111) surface, carbon dioxide was found to adsorb strongly in two configurations on the S-terminated surface, but there was no similar counterpart observed on the Fe-terminated surface.

**Table 2.** Calculated adsorption energy ($E_{ads}$), $CO_2$ inner angle (∡ (O-C-O)), and O-C bond stretching (O1-C/O2-C) of a single $CO_2$ molecule adsorbed on three pristine low Miller index surfaces of FeS mackinawite. The B1 and B2 adsorption position nomenclature were taken from the work of Dzade et al. [24].

| Pristine Surface | Adsorption Position | $E_{ads}$ (eV) | ∡(O-C-O) (°) | O1-C/O2-C Stretching (%) |
|---|---|---|---|---|
| (001)-S | Top Fe | −0.01 | 180.0 | 0.0/0.0 |
| | Top S | −0.01 | 180.0 | 0.0/0.0 |
| (001)-Fe | Top Fe | No stable configuration/surface reconfiguration observed | | |
| | Top S | No stable configuration/surface reconfiguration observed | | |
| (011)-S | Top Fe | −0.23 | 178.6 | 0.7/−0.7 |
| | Top S | 0.01 | 180.0 | 0.0/0.0 |
| (011)-Fe | Top Fe | −0.54 | 138.2 | 6.6/5.9 |
| | Top S | −0.17 | 178.9 | −0.5/0.6 |
| (111)-S | Top Fe | 0.33 | 133.0 | 9.6/2.9 |
| | Top S | No stable config | | |
| | B1 | −0.99 | 133.4 | 5.6/5.6 |
| | B2 | −1.29 | 139.2 | 3.1/5.6 |
| (111)-Fe | Top Fe | No stable configuration/surface reconfiguration observed | | |
| | Top S | No stable configuration/surface reconfiguration observed | | |

For the subsequent study of $CO_2$ adsorption on the Ni-doped surfaces, the pristine surfaces with the strongest adsorption tendency were chosen, namely (001)-S, (011)-Fe, and (111)-S. Ni doping was considered as the case of randomly dispersed substitutional atoms throughout the surface.

As with the undoped surfaces, the $CO_2$ molecule does not adsorb on the Ni-doped (001)-S surface, regardless of the initial placement (complete results listed in Table 3).

**Table 3.** Calculated adsorption energy ($E_{ads}$), $CO_2$ inner angle (∡ (O-C-O)), and O-C bond stretching (O1-C/O2-C) of a single $CO_2$ molecule adsorbed on various Ni-doped surfaces of FeS mackinawite. The B1 and B2 adsorption position nomenclature were taken from the work of Dzade et al. [24]. In the "-alt" notation, the position of the most prominent Fe and Ni atoms was swapped, to test for eventual differences.

| Ni-Doped Surface | Adsorption Position | $E_{ads}$ (eV) | ∡(O-C-O) (°) | O1-C/O2-C Stretching (%) |
|---|---|---|---|---|
| (001)-S | Top Fe | 0.06 | 180.0 | 0.0/0.0 |
| | Top S-1 | 0.07 | 180.0 | 0.0/0.0 |
| | Top S-2 | 0.08 | 180.0 | 0.0/0.0 |
| | Top Ni | 0.06 | 180.0 | 0.0/0.0 |
| (011)-Fe | Top Fe | −0.14 | 148.1 | 6.2/1.9 |
| | Top S | −0.09 | 179.2 | 0.1/−0.1 |
| (111)-S | B1 | 0.14 | 139.5 | 3.1/6.6 |
| | B1-alt | −0.11 | 178.9 | −0.6/0.6 |
| | B2 | −0.53 | 143.9 | 5.7/1.8 |
| | B2-alt | −0.78 | 178.9 | −0.6/0.6 |

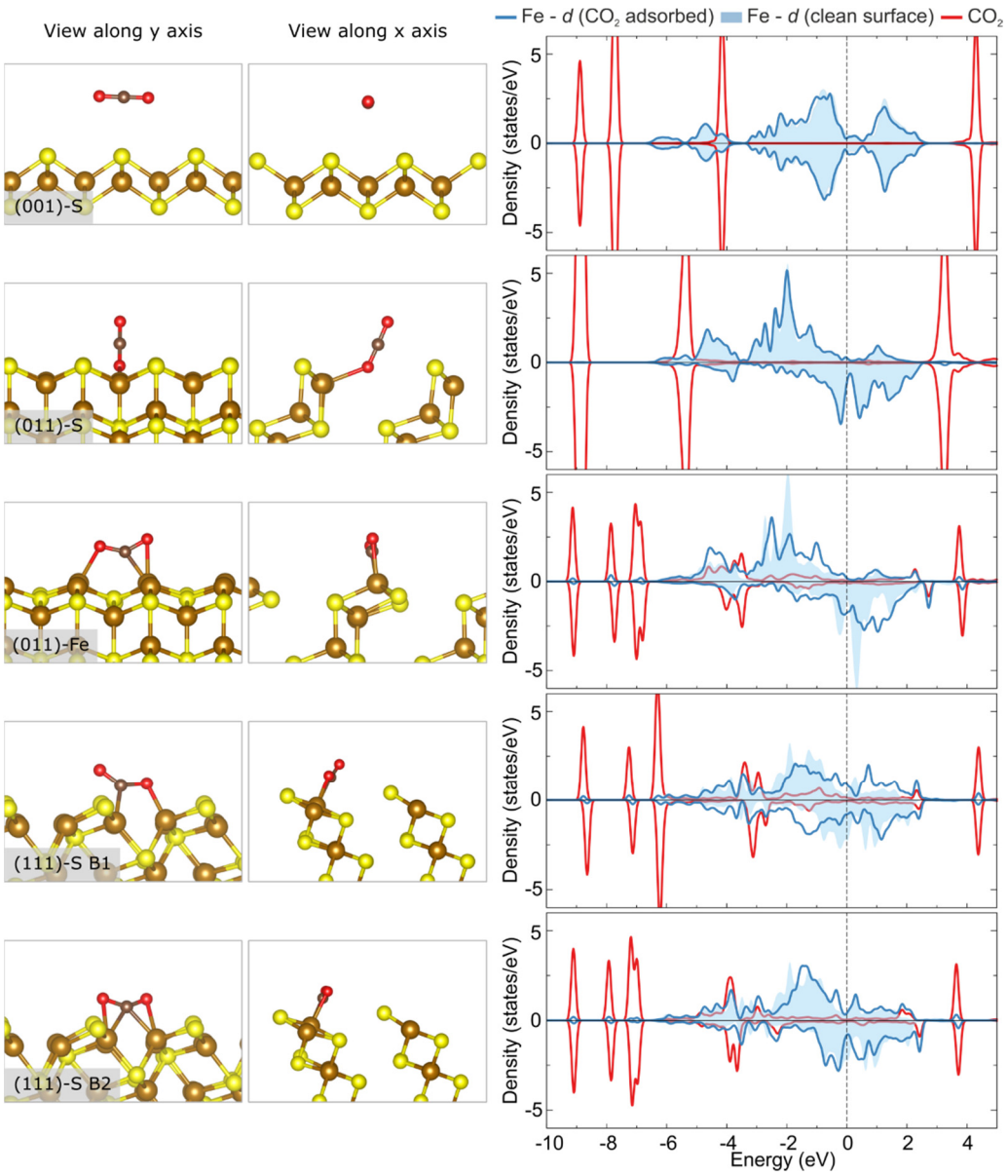


**Figure 4.** Optimised structures of the $CO_2$ molecule adsorbed on the pristine surfaces of FeS (**left**) together with the accompanying electronic densities of the state (**right**).

The adsorption of $CO_2$ on top of the Ni-doped (011) and (111) surfaces is weakened, compared to the undoped surface. Starting from the bridged position of $CO_2$ on the pristine surface, the molecule desorbs from the site where the Ni atom substituted Fe (surface structure depicted in Figure 5). The molecule on top of the (011)-Fe surface rotates away from the Ni atom and stays bound on top of the most prominent Fe atom in an activated state, while $CO_2$ on top of the (111) surface deactivates into a linear conformation, binding weakly to the surface through one of its O atoms.

The changes in the binding mechanism are further illustrated through the calculated electronic densities of state shown in Figure 5. The electronic states of $CO_2$ adsorbed on top of the (001) surface show distinct peaks with negligible changes between the pristine and Ni-doped scenario. In contrast, in the case of the (011) and (111) surfaces, the broadened states overlapping with prominent surface Fe atoms (present around −3 eV) transform into distinct states when Ni is present in the surface.

To quantify the effect of Ni doping onto the surfaces of FeS, the centre of the surface *d*-band was computed, as this property has been linked successfully to understanding

and predicting the catalytic activity of transition metal surfaces [56]. Upon Ni doping, the centre of the *d*-band experiences a downwards shift (average value) of about Δ = 0.25, 0.26, and 0.28 eV in the case of the (001)-S, (011)-Fe, and (111)-S surfaces, respectively. Such a downward shift lowers the possibility to form a large number of empty anti-bonding states, leading to reduced binding energies of the adsorbed $CO_2$ molecule. The reduced number of empty states present in the Ni-doped surface is not necessarily a surprise, considering the increased number of paired electrons in the *d*-states of Ni, compared to the Fe atom, thereby exerting stronger Coulomb repulsion towards the adsorbate.

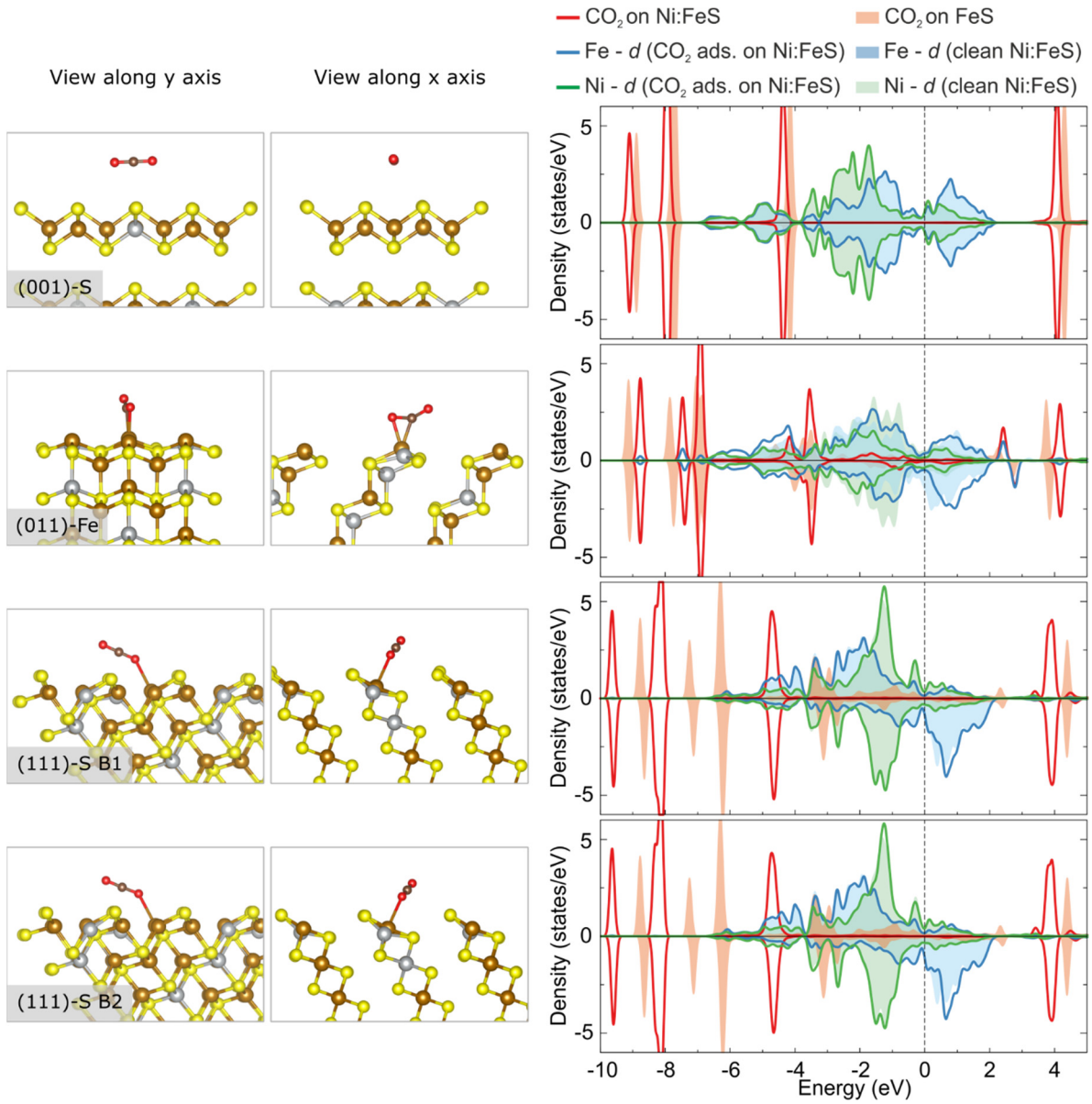


**Figure 5.** Crystal structure of the $CO_2$ molecule adsorbed on the Ni-doped surfaces of FeS (**left**) together with the accompanying electronic densities of the state (**right**).

### *3.4. $CO_2$ Dissociation on Ni-Doped FeS Surfaces*

So far, the influence of Ni on the strength of $CO_2$ adsorption on the surface of FeS has been considered. There is still the question of whether Ni dopants can also dictate the reactivity of the system with respect to $CO_2$ dissociation into surface-bound CO and O species. To analyse this process, the (011)-Fe- and (111)-S-terminated surfaces were

considered for subsequent transition state calculations to obtain reaction energies and activation barriers.

The calculated minimum energy profiles for $CO_2$ dissociation from the chosen starting structures on the (011)-Fe and (111)-S surfaces are shown in Figure 6. The calculated reaction energy at the (011)-Fe surface indicates that the dissociation is an endothermic process with a cost of +0.85 eV. In the final configuration, the dissociated O species binds to a surface S ($d$(O-S) = 1.49 Å) and the remaining CO binds through the C atom to the first prominent Fe atom ($d$(C-Fe) = 1.73 Å). Such behaviour is similar to the one that Dzade et al. [24] observed for $CO_2$ dissociation at a pristine (011) surface. However, the activation energy of 2.39 eV is significantly increased compared to the 1.25 eV calculated for the same process occurring at an undoped surface.

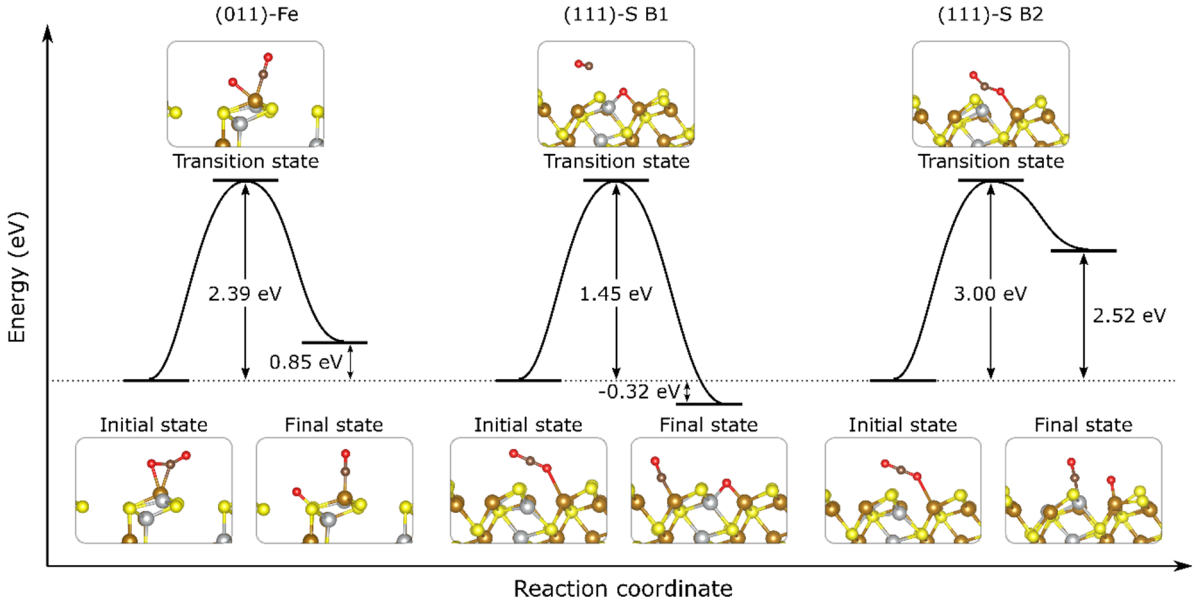


**Figure 6.** Calculated potential energy profile for $CO_2$ dissociation on Ni-doped FeS mackinawite surfaces.

The situation at the (111)-S surface is quite different. Splitting $CO_2$ into CO + O starting from the B1 position outlined earlier proceeds as an exothermic reaction releasing 0.32 eV in energy, with a final configuration where O bridges one Fe and one Ni atom and CO attaches to an adjacent Fe atom but avoiding the most prominent Ni atom. The activation energy is calculated at 1.45 eV, which is a value that is doubled compared to the 0.72 eV for $CO_2$ dissociation on top of an undoped (111)-S surface.

In contrast, splitting of $CO_2$ from the initial B2 position on the (111)-S surface proceeds towards a state where the CO moiety weakly interacts atop a Ni atom and the remaining O binds to a prominent Fe atom. The C-Ni bond length is measured at 1.84 Å, which contrasts with the C-Fe bond length of 1.76 Å, indicating a weaker interaction when compared to the $CO_2$ split from the B1 configuration. The calculated reaction energy reveals that this process is highly endothermic, requiring +2.52 eV to materialise, further confirming the reduced impact Ni plays in the catalytic properties of mackinawite. The activation energy is calculated at almost 3 eV, rendering this dissociation scenario highly unfavourable.

## 4. Conclusions

A computational study of the effect of substitutional Ni doping on the most prominent surfaces of FeS mackinawite was undertaken using DFT-D3 calculations. Three different doping patterns were studied for Ni incorporated at the Fe site as well as the possible effect of the dopant on the adsorption and activation of $CO_2$. Following the results presented above, several significant conclusions can be drawn:

a Ni is readily incorporated substitutionally at the Fe site into the FeS matrix, where low formation energies indicate that it may be difficult to control the dopant concentration.
b FeS surfaces doped with Ni exhibit weaker binding as well as deactivation of adsorbed CO2 molecules, when compared to the same process on undoped mackinawite surfaces.
c The (average) position of the d-band centre of the Ni-doped surfaces of FeS mackinawite is found at a consistently lower position than it is at the pristine surfaces. This is linked to the electronic configuration of Ni atoms, which is closer to a closed-shell system than that of the open d-orbitals of Fe atoms.

The results presented here indicate a reduced activity of Ni-doped surfaces of FeS mackinawite towards the possible activation and dissociation of $CO_2$. However, care should be taken when interpreting these results, as certain limitations apply. The system under scrutiny was subjected neither to varying temperatures and pressures, nor has it included competitive adsorbates such as water or oxygen, which are known to have a strong effect on the stability of mackinawite [28,32]. For example, in a recent work, Hudson et al. [57] reported reduction of $CO_2$ with $H_2$ to formate ($HCOO^-$) across Fe(Ni)S precipitates. Direct comparison with such works is very difficult, owing to the vast number of variables not available in the presented study, such as pH and redox gradients. More importantly, Dzade et al. [58] unravelled the role that sulphur vacancies play in promoting $CO_2$ and $H_2$ adsorption on the FeS(001) basal plane. It would be of considerable interest to include sulphur and iron vacancies together with Ni dopants in a follow-up work to probe their synergic effect onto the adsorption properties of FeS surfaces. Nevertheless, this study was able to probe the isolated effect of pure Ni doping onto the catalytic properties of mackinawite and unravel some of the roles that Ni incorporation could play in the diverse group of iron sulphide solids.

**Supplementary Materials:** The following are available online at https://www.mdpi.com/article/10.3390/catal11040486/s1.

**Author Contributions:** Conceptualization, A.Ž., E.C., and M.W.; methodology, A.Ž., M.W., N.H.d.L.; validation, A.Ž., M.S., E.C., H.E.K., M.W., and N.H.d.L.; investigation and data curation, A.Ž. and M.S.; writing—original draft preparation, A.Ž.; writing—review and editing, A.Ž., M.S., E.C., H.E.K., M.W., and N.H.d.L.; supervision, M.W. and E.C. All authors have read and agreed to the published version of the manuscript.

**Funding:** A.Ž. and N.H.d.L acknowledge the NWO ECHO grant (712.018.005) for funding. E.C. acknowledges NWO and the Dutch Origins Center for funding. This project has received funding from the European Research Council (ERC) under the European Union's Horizon 2020 research and innovation programme (grant agreement No 819588).

**Acknowledgments:** Part of the local compute cluster and the research work of M.W. is part of the Industrial Partnership Programme i32 Computational Sciences for Energy Research that is carried out under an agreement between Shell and the Netherlands Organisation for Scientific Research (NWO). This work was carried out on the Dutch national e-infrastructure with the support of SURF Cooperative.

**Conflicts of Interest:** The authors declare no conflict of interest.

## References

1. Handoko, A.D.; Wei, F.; Yeo, B.S.; Seh, Z.W. Understanding heterogeneous electrocatalytic carbon dioxide reduction through operando techniques. *Nat. Catal.* **2018**, *1*, 922–934. [CrossRef]
2. Wansleben, M.; Vinson, J.; Wählisch, A.; Bzheumikhova, K.; Hönicke, P.; Beckhoff, B.; Kayser, Y. Speciation of iron sulfide compounds by means of X-ray emission spectroscopy using a compact full-cylinder von Hamos spectrometer. *J. Anal. At. Spectrom.* **2020**, *35*, 2679–2685. [CrossRef]
3. Yang, X.; Wang, D. From Fundamental Principles to Materials and Applications. *ACS Appl. Energy Mater.* **2018**, *1*, 6657–6693. [CrossRef]
4. Graves, C.; Ebbesen, S.D.; Mogensen, M.; Lackner, K.S. Sustainable hydrocarbon fuels by recycling $CO_2$ and $H_2O$ with renewable or nuclear energy. *Renew. Sustain. Energy Rev.* **2011**, *15*, 1–23. [CrossRef]

5. Xu, S.; Carter, E.A. Theoretical Insights into Heterogeneous (Photo)electrochemical $CO_2$ Reduction. *Chem. Rev.* **2019**, *119*, 6631–6669. [CrossRef] [PubMed]
6. Rafiee, A.; Khalilpour, K.R.; Milani, D.; Panahi, M. Trends in $CO_2$ conversion and utilization: A review from process systems perspective. *J. Environ. Chem. Eng.* **2018**, *6*, 5771–5794. [CrossRef]
7. Seh, Z.W.; Kibsgaard, J.; Dickens, C.F.; Chorkendorff, I.; Nørskov, J.K.; Jaramillo, T.F. Combining theory and experiment in electrocatalysis: Insights into materials design. *Science* **2017**, *355*, eaad4998. [CrossRef] [PubMed]
8. Vaughan, D.J.; Becker, U.; Wright, K. Sulphide mineral surfaces: Theory and experiment. *Int. J. Miner. Process.* **1997**, *51*, 1–14. [CrossRef]
9. Vaughan, D.J. Sulfide Mineralogy and Geochemistry: Introduction and Overview. *Rev. Mineral. Geochem.* **2006**, *61*, 1–5. [CrossRef]
10. Inosov, D.S. Quantum magnetism in minerals. *Adv. Phys.* **2018**, *67*, 149–252. [CrossRef]
11. Rickard, D.; Luther, G.W. Chemistry of Iron Sulfides. *Chem. Rev.* **2007**, *107*, 514–562. [CrossRef] [PubMed]
12. Huber, C. Peptides by Activation of Amino Acids with CO on (Ni,Fe)S Surfaces: Implications for the Origin of Life. *Science* **1998**, *281*, 670–672. [CrossRef]
13. Drobner, E.; Huber, H.; Wächtershäuser, G.; Rose, D.; Stetter, K.O. Pyrite formation linked with hydrogen evolution under anaerobic conditions. *Nature* **1990**, *346*, 742–744. [CrossRef]
14. Russell, M.J.; Daniel, R.M.; Hall, A.J.; Sherringham, J.A. A hydrothermally precipitated catalytic iron sulphide membrane as a first step toward life. *J. Mol. Evol.* **1994**, *39*, 231–243. [CrossRef]
15. Roldan, A.; Hollingsworth, N.; Roffey, A.; Islam, H.U.; Goodall, J.B.M.; Catlow, C.R.A.; Darr, J.A.; Bras, W.; Sankar, G.; Holt, K.B.; et al. Bio-inspired $CO_2$ conversion by iron sulfide catalysts under sustainable conditions. *Chem. Commun.* **2015**, *51*, 7501–7504. [CrossRef] [PubMed]
16. Herschy, B.; Whicher, A.; Camprubi, E.; Watson, C.; Dartnell, L.; Ward, J.; Evans, J.R.G.; Lane, N. An Origin-of-Life Reactor to Simulate Alkaline Hydrothermal Vents. *J. Mol. Evol.* **2014**, *79*, 213–227. [CrossRef]
17. Terranova, U.; Mitchell, C.; Sankar, M.; Morgan, D.; De Leeuw, N.H. Initial Oxygen Incorporation in the Prismatic Surfaces of Troilite FeS. *J. Phys. Chem. C* **2018**, *122*, 12810–12818. [CrossRef]
18. Hu, Y.; Wu, G.; Li, R.; Xiao, L.; Zhan, X. Iron sulphides mediated autotrophic denitrification: An emerging bioprocess for nitrate pollution mitigation and sustainable wastewater treatment. *Water Res.* **2020**, *179*, 115914. [CrossRef]
19. Li, Q.; Zhang, Y.; Liao, Y.; Huang, J.; Dang, Z.; Guo, C. Removal of hexavalent chromium using biogenic mackinawite (FeS)-deposited kaolinite. *J. Colloid Interface Sci.* **2020**, *572*, 236–245. [CrossRef] [PubMed]
20. Vessey, C.J.; Lindsay, M.B.J. Aqueous Vanadate Removal by Iron(II)-Bearing Phases under Anoxic Conditions. *Environ. Sci. Technol.* **2020**, *54*, 4006–4015. [CrossRef] [PubMed]
21. Cody, G.D.; Boctor, N.Z.; Brandes, J.A.; Filley, T.R.; Hazen, R.M.; Yoder, H.S. Assaying the catalytic potential of transition metal sulfides for abiotic carbon fixation. *Geochim. Cosmochim. Acta* **2004**, *68*, 2185–2196. [CrossRef]
22. Dzade, N.Y.; Roldan, A.; De Leeuw, N.H. The surface chemistry of NOx on mackinawite (FeS) surfaces: A DFT-D2 study. *Phys. Chem. Chem. Phys.* **2014**, *16*, 15444–15456. [CrossRef] [PubMed]
23. Dzade, N.Y.; Roldan, A.; De Leeuw, N.H. Adsorption of methylamine on mackinawite (FES) surfaces: A density functional theory study. *J. Chem. Phys.* **2013**, *139*, 124708. [CrossRef] [PubMed]
24. Dzade, N.Y.; Roldan, A.; De Leeuw, N.H. Activation and dissociation of $CO_2$ on the (001), (011), and (111) surfaces of mackinawite (FeS): A dispersion-corrected DFT study. *J. Chem. Phys.* **2015**, *143*, 094703. [CrossRef] [PubMed]
25. Dzade, N.Y.; Roldan, A.; De Leeuw, N.H. Structures and Properties of $As(OH)_3$ Adsorption Complexes on Hydrated Mackinawite (FeS) Surfaces: A DFT-D2 Study. *Environ. Sci. Technol.* **2017**, *51*, 3461–3470. [CrossRef]
26. Dzade, N.Y.; Roldan, A.; De Leeuw, N.H. Surface and shape modification of mackinawite (FeS) nanocrystals by cysteine adsorption: A first-principles DFT-D2 study. *Phys. Chem. Chem. Phys.* **2016**, *18*, 32007–32020. [CrossRef]
27. Dzade, N.Y.; Roldan, A.; De Leeuw, N.H. DFT-D2 simulations of water adsorption and dissociation on the low-index surfaces of mackinawite (FeS). *J. Chem. Phys.* **2016**, *144*, 174704. [CrossRef]
28. Dzade, N.Y.; Roldan, A.; De Leeuw, N.H. DFT-D2 study of the adsorption and dissociation of water on clean and oxygen-covered {001} and {011} surfaces of mackinawite (FeS). *J. Phys. Chem. C* **2016**, *120*, 21441–21450. [CrossRef]
29. Kolos, M.; Tunega, D.; Karlický, F. A theoretical study of adsorption on iron sulfides towards nanoparticle modeling. *Phys. Chem. Chem. Phys.* **2020**, *22*, 23258–23267. [CrossRef]
30. Ofili, N.E.R.; Thetford, A.; Kaltsoyannis, N. Adsorption of U(VI) on Stoichiometric and Oxidised Mackinawite: A DFT Study. *Environ. Sci. Technol.* **2020**, *54*, 6792–6799. [CrossRef]
31. Hu, Q.; Wang, C.; Geng, Y.; Zhang, X.; Mei, J.; Yang, S. Remarkable differences between copper-based sulfides and iron-based sulfides for the adsorption of high concentrations of gaseous elemental mercury: Mechanisms, kinetics, and significance. *J. Colloid Interface Sci.* **2021**, *582*, 581–590. [CrossRef]
32. Morse, J.W.; Arakaki, T. Adsorption and coprecipitation of divalent metals with mackinawite (FeS). *Geochim. Cosmochim. Acta* **1993**, *57*, 3635–3640. [CrossRef]
33. Kwon, K.D.; Refson, K.; Sposito, G. Transition metal incorporation into mackinawite (tetragonal FeS). *Am. Mineral.* **2015**, *100*, 1509–1517. [CrossRef]
34. Wilkin, R.T.; Beak, D.G. Uptake of nickel by synthetic mackinawite. *Chem. Geol.* **2017**, *462*, 15–29. [CrossRef] [PubMed]

35. Ikogou, M.; Ona-Nguema, G.; Juillot, F.; Le Pape, P.; Menguy, N.; Richeux, N.; Guigner, J.M.; Noël, V.; Brest, J.; Baptiste, B.; et al. Long-term sequestration of nickel in mackinawite formed by Desulfovibrio capillatus upon Fe(III)-citrate reduction in the presence of thiosulfate. *Appl. Geochemistry* **2017**, *80*, 143–154. [CrossRef]
36. Swanner, E.D.; Webb, S.M.; Kappler, A. Fate of cobalt and nickel in mackinawite during diagenetic pyrite formation. *Am. Mineral.* **2019**, *104*, 917–928. [CrossRef]
37. Kresse, G.; Joubert, D. From ultrasoft pseudopotentials to the projector augmented-wave method. *Phys. Rev. B* **1999**, *59*, 1758–1775. [CrossRef]
38. Kresse, G.; Furthmüller, J. Efficient iterative schemes for ab initio total-energy calculations using a plane-wave basis set. *Phys. Rev. B* **1996**, *54*, 11169–11186. [CrossRef] [PubMed]
39. Kresse, G.; Furthmüller, J. Efficiency of ab-initio total energy calculations for metals and semiconductors using a plane-wave basis set. *Comput. Mater. Sci.* **1996**, *6*, 15–50. [CrossRef]
40. Perdew, J.P.; Burke, K.; Ernzerhof, M. Generalized Gradient Approximation Made Simple. *Phys. Rev. Lett.* **1996**, *77*, 3865–3868. [CrossRef]
41. Grimme, S.; Antony, J.; Ehrlich, S.; Krieg, H. A consistent and accurate ab initio parametrization of density functional dispersion correction (DFT-D) for the 94 elements H-Pu. *J. Chem. Phys.* **2010**, *132*, 154104. [CrossRef] [PubMed]
42. Monkhorst, H.J.; Pack, J.D. Special points for Brillouin-zone integrations. *Phys. Rev. B* **1976**, *13*, 5188–5192. [CrossRef]
43. Yu, M.; Trinkle, D.R. Accurate and efficient algorithm for Bader charge integration. *J. Chem. Phys.* **2011**, *134*, 064111. [CrossRef] [PubMed]
44. Tang, W.; Sanville, E.; Henkelman, G. A grid-based Bader analysis algorithm without lattice bias. *J. Phys. Condens. Matter* **2009**, *21*, 084204. [CrossRef] [PubMed]
45. Sanville, E.; Kenny, S.D.; Smith, R.; Henkelman, G. Improved grid-based algorithm for Bader charge allocation. *J. Comput. Chem.* **2007**, *28*, 899–908. [CrossRef]
46. Momma, K.; Izumi, F. VESTA 3 for three-dimensional visualization of crystal, volumetric and morphology data. *J. Appl. Crystallogr.* **2011**, *44*, 1272–1276. [CrossRef]
47. Wang, V.; Xu, N.; Liu, J.C.; Tang, G.; Geng, W.-T. VASPKIT: A Pre- and Post-Processing Program for VASP code. *arXiv* **2019**, arXiv:1908.08269.
48. Sheppard, D.; Terrell, R.; Henkelman, G. Optimization methods for finding minimum energy paths. *J. Chem. Phys.* **2008**, *128*, 134106.
49. Henkelman, G.; Jónsson, H. Improved tangent estimate in the nudged elastic band method for finding minimum energy paths and saddle points. *J. Chem. Phys.* **2000**, *113*, 9978–9985. [CrossRef]
50. Henkelman, G.; Uberuaga, B.P.; Jónsson, H. A climbing image nudged elastic band method for finding saddle points and minimum energy paths. *J. Chem. Phys.* **2000**, *113*, 9901–9904. [CrossRef]
51. Freysoldt, C.; Grabowski, B.; Hickel, T.; Neugebauer, J.; Kresse, G.; Janotti, A.; Van De Walle, C.G. First-principles calculations for point defects in solids. *Rev. Mod. Phys.* **2014**, *86*, 253–305. [CrossRef]
52. Watson, G.W.; Kelsey, E.T.; De Leeuw, N.H.; Harris, D.J.; Parker, S.C. Atomistic simulation of dislocations, surfaces and interfaces in MgO. *J. Chem. Soc. Faraday Trans.* **1996**, *92*, 433. [CrossRef]
53. Farkaš, B.; Santos-Carballal, D.; Cadi-Essadek, A.; De Leeuw, N.H. A DFT+U study of the oxidation of cobalt nanoparticles: Implications for biomedical applications. *Materialia* **2019**, *7*, 100381. [CrossRef]
54. Wolthers, M.; Van Der Gaast, S.J.; Rickard, D. The structure of disordered mackinawite. *Am. Mineral.* **2003**, *88*, 2007–2015. [CrossRef]
55. Mansor, M.; Winkler, C.; Hochella, M.F.; Xu, J. Nanoparticulate Nickel-Hosting Phases in Sulfidic Environments: Effects of Ferrous Iron and Bacterial Presence on Mineral Formation Mechanism and Solid-Phase Nickel Distribution. *Front. Earth Sci.* **2019**, *7*, 151. [CrossRef]
56. Hammer, B.; Nørskov, J.K. Theoretical surface science and catalysis—calculations and concepts. *Adv. Catal.* **2000**, *45*, 71–129.
57. Hudson, R.; De Graaf, R.; Rodin, M.S.; Ohno, A.; Lane, N.; McGlynn, S.E.; Yamada, Y.M.A.; Nakamura, R.; Barge, L.M.; Braun, D.; et al. $CO_2$ reduction driven by a pH gradient. *Proc. Natl. Acad. Sci. USA* **2020**, *117*, 22873–22879. [CrossRef] [PubMed]
58. Dzade, N.Y.; De Leeuw, N.H. Activating the FeS (001) Surface for $CO_2$ Adsorption and Reduction through the Formation of Sulfur Vacancies: A DFT-D3 Study. *Catalysts* **2021**, *11*, 127. [CrossRef]